

Real-Space Imaginary-Time Propagators for Non-Local Nucleon-Nucleon Potentials

J.E. Lynn* and K.E. Schmidt†

Department of Physics, Arizona State University, Tempe, Arizona, 85287, USA

(Dated: November 27, 2024)

Abstract

Nuclear structure quantum Monte Carlo methods such as Green's function or auxiliary field diffusion Monte Carlo have used phenomenological local real-space potentials containing as few derivatives as possible, such as the Argonne-Urbana family of interactions, to make sampling simple and efficient. Basis set methods such as no-core shell model and coupled-cluster techniques typically use softer non-local potentials because of their more rapid convergence with basis set size. These non-local potentials are usually defined in momentum space and are often based on effective field theory. Comparisons of the results of the two types of methods can be difficult when different potentials are used. We show methods for evaluating the real-space imaginary-time propagators needed to perform quantum Monte Carlo calculations using such non-local potentials. We explore the universality of the large imaginary time propagators for different potentials and discuss how non-local potentials can be used in quantum Monte Carlo calculations.

PACS numbers: 21.60.Ka, 21.30.-x, 13.75.Cs

* joel.lynn@asu.edu

† kevin.schmidt@asu.edu

I. INTRODUCTION

Quantum chromodynamics (QCD) is the fundamental theory that underlies the description of atomic nuclei, where quarks and gluons are the degrees of freedom. However, despite four decades of studying QCD, little connection has been made between QCD and low-energy many-body nuclear dynamics. The most direct computational application of QCD, lattice QCD, has made much progress in the past decades but remains some distance away from being a practical tool for computing many-body nuclear observables. For recent reviews of the outlook for lattice QCD calculations as they apply to nuclear physics see Refs. [1, 2]. While direct applications of effective field theory have made progress [3–6] the characterization of atomic nuclei in terms of phenomenological two- and three-body nucleon interactions remains the standard starting point for most nuclear structure calculations.

Quantum Monte Carlo is one of the most successful methods for nuclear matter and nuclear structure calculations. Green’s function Monte Carlo has solved for many low lying states of nuclei for $A \leq 12$ [7, 8] and auxiliary-field diffusion Monte Carlo can calculate much larger nuclei and nuclear and neutron matter [9–11]. These methods have used phenomenological local real-space potentials containing as few derivatives as possible, such as the Argonne-Urbana family of interactions [12–14], to make sampling easy and efficient. See Ref. [8] for a review of Green’s function Monte Carlo results.

However, there are other successful approaches that can reach $A = 12$ and beyond. Basis-set methods such as the no-core shell model [15, 16] and coupled-cluster techniques [17–19] have typically used softer non-local potentials as these have more rapid convergence with basis-set size. These potentials are typically defined in momentum space and are often derived from chiral effective field theory such as the next-to-next-to-next-to-leading order (N^3LO) interaction of Ref. [20].

Comparison of the results of basis set methods with Monte Carlo calculations can be difficult when different potentials are used. Quantum Monte Carlo methods use propagation in imaginary time to project out the low-energy states of a quantum many-particle system. The propagation is performed by first writing the many-body short-imaginary-time propagator. Accurate methods use a pair-product approximation [21, 22] where the many-body propagator is written in terms of the propagator for each pair of particles. In order to perform a quantum Monte Carlo calculation using an arbitrary pair potential, we need to

calculate the pair propagator in imaginary time.

The aim of this paper is to show how to evaluate this real-space imaginary-time pair propagator needed to perform quantum Monte Carlo calculations using non-local potentials (Sec. II), to demonstrate the consistency of the propagators using different potentials at large imaginary times (Sec. III), and to discuss how to use these propagators to calculate the properties of nuclei and nuclear matter using these non-local potentials with quantum Monte Carlo methods (Sec. IV).

II. METHODS

Non-local potentials are typically generated in momentum space from an effective field theory. With a potential defined in momentum space, $V(k, k')$, it is natural that we proceed by constructing a Hamiltonian in momentum space as well. Our normalization and completeness conventions for our continuous real-space and momentum-space basis states are

$$1 = \int d^3r |\mathbf{r}\rangle \langle \mathbf{r}| = \int \frac{d^3k}{(2\pi)^3} |\mathbf{k}\rangle \langle \mathbf{k}|. \quad (1)$$

\mathbf{r} is the separation vector of the two nucleons and $\mathbf{p} = \hbar\mathbf{k}$ the conjugate momentum. The overlaps between the states are

$$\langle \mathbf{r} | \mathbf{k} \rangle = e^{i\mathbf{k} \cdot \mathbf{r}}. \quad (2)$$

We work in the standard channel basis where J^2 , J_z , L^2 , S^2 , S_z , T^2 and T_z are good quantum numbers, with the total spin, $\mathbf{S} = \mathbf{S}_1 + \mathbf{S}_2$, the total angular momentum $\mathbf{J} = \mathbf{L} + \mathbf{S}$, and total isospin $\mathbf{T} = \mathbf{T}_1 + \mathbf{T}_2$. We choose our basis states as $|rJMLSTT_z\rangle$ and $|kJMLSTT_z\rangle$, with normalization and completeness given by (suppressing J , S , T , and T_z)

$$\begin{aligned} 1 &= \sum_{LM} \int_0^\infty r^2 dr |rLM\rangle \langle rLM| \\ &= \sum_{LM} \int_0^\infty \frac{k^2 dk}{(2\pi)^3} |kLM\rangle \langle kLM|. \end{aligned} \quad (3)$$

The overlaps are

$$\langle rLM | kL'M' \rangle = 4\pi i^L j_L(kr) \delta_{LL'} \delta_{MM'}. \quad (4)$$

For numerical work, we compactify our real space to a sphere of radius R . We choose the Dirichlet boundary condition on the sphere which forces our momentum-space spectrum

to be discrete with $k_n^{(L)}R$ being the zeros of the spherical Bessel functions, $j_L(k_n^{(L)}R) = 0$. Below we often drop the superscript (L) when its value is clear from context. The discrete momentum states $|k_nLM\rangle$ are chosen with unit normalization so that

$$\langle rLM|k_nL'M'\rangle = \sqrt{\frac{2}{R^3 j_L'(k_n R)^2}} j_L(k_n r) \delta_{LL'} \delta_{MM'}. \quad (5)$$

Our transformations can now be treated as orthogonal-matrix multiplications.

The momentum-space Hamiltonian for the uncoupled channels where $L = J$ (for a given set of the quantum numbers — J , M , L , S , T , and T_z — which we suppress below) is

$$\langle k_m|H|k_n\rangle = \frac{\hbar^2 k_n^2}{2m_r} \delta_{mn} + V(k_m, k_n), \quad (6)$$

with m_r the reduced mass. For the coupled channels where the potentials couple the $L = J \pm 1$ states together the Hamiltonian is

$$\langle k_m L|H|k_n L'\rangle = \begin{pmatrix} \frac{\hbar^2 k_n^{(-)2}}{2m_r} \delta_{mn} + V_{--}(k_m^{(-)}, k_n^{(-)}) & V_{-+}(k_m^{(-)}, k_n^{(+)}) \\ V_{+-}(k_m^{(+)}, k_n^{(-)}) & \frac{\hbar^2 k_n^{(+2}}{2m_r} \delta_{mn} + V_{++}(k_m^{(+)}, k_n^{(+)}) \end{pmatrix}, \quad (7)$$

where the superscripts $(-)$ and $(+)$ correspond to L or L' having values of $J - 1$ and $J + 1$. We then construct the momentum-space, imaginary-time propagator by diagonalization of the Hamiltonian, giving

$$\langle k_m|e^{-H\tau}|k_n\rangle = \sum_{i=1}^{N_k} \langle k_m|\psi_i\rangle e^{-E_i\tau} \langle \psi_i|k_n\rangle, \quad (8)$$

for the uncoupled channels, and

$$\langle k_m L|e^{-H\tau}|k_n L'\rangle = \sum_{i=1}^{N_k} \langle k_m L|\psi_i\rangle e^{-E_i\tau} \langle \psi_i|k_n L'\rangle, \quad (9)$$

for the coupled channels. The $\{|\psi_i\rangle\}$ are eigenvectors of the Hamiltonian with corresponding eigenvalues $\{E_i\}$. N_k is the number of discrete momentum states we keep. We ensure that N_k is large enough such that the propagators converge. An estimate of how large k_{\max} should be can be given by considering the kinetic energy alone. We want k_{\max} such that $\exp\left(-\frac{\hbar^2 k_{\max}^2}{2m} \tau\right)$ can be neglected. In practice, we check the convergence by doubling our estimate for k_{\max} and ensuring our results do not change to the desired precision. With these methods, it is easy to ensure that the numerical truncation errors are completely

negligible. For example, for the results shown here, we use $k_{\max} = 40 \text{ fm}^{-1}$ ($N_k \sim 80$), and the propagators have truncation errors less than 10^{-10} .

After transforming to real space, we have the matrix elements

$$\langle rJMLSTT_z | e^{-H\tau} | r'JML'STT_z \rangle. \quad (10)$$

However, for use in Monte Carlo codes, we want the propagators in a 3D real-space basis, $|r\theta\phi SM_S TT_z\rangle$,

$$|r\theta\phi SM_S TT_z\rangle = \sum_{JMLM_L} C_{SM_S LM_L}^{JM} Y_{LM_L}(\theta, \phi) |rJMLSTT_z\rangle. \quad (11)$$

C is a Clebsch-Gordan coefficient, Y a spherical harmonic.

In quantum Monte Carlo calculations, the particle positions are typically sampled from the central part of the propagator. The non-central parts are then included in the spin-isospin samples (auxiliary field diffusion Monte Carlo) or sums (Green's function Monte Carlo). We will sample the propagators for these non-local potentials in the same way. Here, we define the central part of the propagator as the trace over all spins and isospins. For convenience we also choose a particular coordinate system where the initial separation lies along the z axis, and the final separation is in the xz plane such that we may take $\theta = \phi = \phi' = 0$ and we can visualize the central part of the propagator as a function of $r - r'$ and θ' . For any particular application, we can always rotate into this configuration, propagate, and rotate back. The central part of the propagator is then written as

$$G(r, r', \theta'; \tau) = \sum_{SM_S TT_z} \langle r SM_S TT_z | e^{-H\tau} | r' \theta' SM_S TT_z \rangle. \quad (12)$$

III. CONSISTENCY OF THE PROPAGATORS AT LARGE IMAGINARY TIMES

In the limit of large imaginary times, we expect that the propagators for different potentials should agree. The propagators are essentially density matrices for the two nucleon system:

$$\rho = \frac{\sum_i |\psi_i\rangle e^{-E_i\tau} \langle \psi_i|}{\sum_i e^{-E_i\tau}}; \quad \text{tr} \rho = 1, \quad (13)$$

corresponding to thermal equilibrium at the temperature $k_B T = \tau^{-1}$. Now, since any measurable quantity can be written as an expectation of a Hermitian operator O which can be obtained via $\langle O \rangle = \text{tr}(\rho O)$, the density matrices (propagators) we obtain for the

various potentials contain all the measurable information for this system. If the position or momentum of the nucleons could be determined with arbitrary precision, the density matrix would be in principle measurable. Since the position and momentum are not well defined for arbitrary values, the propagator is not completely measurable. If the various potentials we use are phase-shift equivalent — meaning they reproduce the physical scattering data at or below $E_{\text{lab}} \approx 350$ MeV ($E_{\text{c.m.}} \approx 175$ MeV) — then we would expect that starting at imaginary times $\tau \approx (175 \text{ MeV})^{-1}$, the various propagators should begin to agree more and more. In fact, we find that for $\tau \approx (50 \text{ MeV})^{-1}$, the higher-energy modes not constrained by current experimental data do not contribute substantially to the propagator.

We see from Eq. (13) that at $\tau \approx (175 \text{ MeV})^{-1}$, energies of 175 MeV and above are suppressed by a factor of $1/e$. Therefore, it is not surprising that at $\tau \approx (50 \text{ MeV})^{-1}$, where energies of 175 MeV and above are suppressed by a factor of $1/e^3 \approx 0.0498$ we find relatively good agreement between the propagators with different potentials. This result is analogous to the renormalization group results leading to the $V_{\text{low } k}$ potential of Ref. [23] and the similarity renormalization group results of Ref. [24], where the high energy modes are integrated out.

Figures 1–9 demonstrate these findings for three potentials: Argonne v_{18} (AV_{18}) [12], $N^3\text{LO}$, and $N^3\text{LO}(600)$ [20]. For the diagonal cases, where we take $k = k'$, we define a quantum potential, $V_q(k, k; \tau)$ through the equation

$$\langle k | e^{-H\tau} | k \rangle = \langle k | e^{-H_0 \frac{\tau}{2}} e^{-V_q(k, k; \tau)} e^{-H_0 \frac{\tau}{2}} | k \rangle, \quad (14)$$

with H_0 the free-particle Hamiltonian

$$H_0 = T = \frac{p^2}{2m}. \quad (15)$$

In the off-diagonal cases ($k \neq k'$) we choose a particular k value and plot against k' . For visual comparison, we subtract the free-particle propagator, $g(k, k') - g_0(k, k')$, since at the point $k = k'$, the kinetic energy component is large and obscures the result.

Figures 1–4 show the quantum potential in the singlet (1S_0), uncoupled triplet (3P_0), and coupled triplet (3S_1 and 3D_1) channels. The imaginary times chosen correspond to a typical time step used in Green’s function Monte Carlo calculations, $\tau = (2000 \text{ MeV})^{-1}$ and imaginary times that roughly correspond to center-of-mass energies of 350 MeV, 175 MeV, and 50 MeV. As we have discussed above, the imaginary time of $\tau = (50 \text{ MeV})^{-1}$ is the time

at which the effects attributable to energies of 175 MeV and above are effectively integrated out. It is interesting to note that the agreement of the quantum potentials is only good up to $k \approx 2 \text{ fm}^{-1}$: this is the approximate momentum value, k , one would associate with the corresponding kinetic energy: $\frac{\hbar^2 k^2}{2m} = 175 \text{ MeV}$. This relationship (better and better agreement — but only up to some cut off — as the potential is evolved) is precisely what is found in similarity renormalization group and $V_{\text{low } k}$ approaches.

It is tempting to interpret τ as an evolution parameter for the quantum potential in the same sense that the similarity renormalization group approach has s or λ (see, for example, [24]). However, it is not clear if a direct comparison is at all trivial. In the similarity renormalization group approach, the evolution parameter s (and therefore λ , since $\lambda = 1/s^{1/4}$) is defined through the rather simple evolution equation for the potential

$$\frac{dH_s}{ds} = \frac{dV_s}{ds} = [[G_s, H_s], H_s], \quad (16)$$

where G_s is a Hermitian operator that generates the transformation. (G_s is often chosen to be T , the kinetic energy). If we view our quantum potential akin to the similarity renormalization group's V_s , our defining equation is

$$e^{-H\tau} = e^{-T\frac{\tau}{2}} e^{-V_q(\tau)\tau} e^{-T\frac{\tau}{2}}. \quad (17)$$

We can expand this using the Baker-Campbell-Hausdorff relation which gives an infinite series of nested commutators. The lowest order terms in an expansion in τ are

$$V_q(\tau) = V - \frac{\tau^2}{12} ([V, [V, T]] - \frac{1}{2}[T, [T, V]]) + \dots \quad (18)$$

where the double commutators are suggestive of Eq. (16), but clearly not the same. The differential equation satisfied by $V_q(\tau)$ is not a simple, compact expression.

Figures 5-9, show the off-diagonal elements of the singlet (1S_0), uncoupled triplet, (3P_0), and coupled triplet (3S_1 , 3D_1 , and 3S_1 - 3D_1) channel propagators. As discussed above, they are shifted by the free-particle result to make comparisons easier. What we can see from these figures is a general trend towards universality with at least two caveats. First, the propagators tend to converge most rapidly around the point where $k = k'$. Our interpretation of this result is that low momentum transfer behavior is constrained by the phase-shift equivalence of the various potentials whereas higher momentum transfer behavior is not. Second, some channels converge better than others. For example, Fig. 8 has still not converged

at $\tau = (50 \text{ MeV})^{-1}$, and indeed, does not appear to converge well until $\tau = (10 \text{ MeV})^{-1}$. This may be due to this channel's sensitivity to the tensor part of the interaction which the different potentials treat differently. These differences may point to true, quantifiable distinctions between the potentials.

Even though the potentials give propagators with the same sort of long imaginary time behavior, the many-body physics of the nucleus may not allow the use of the propagators in this regime. As mentioned above, in Green's function Monte Carlo calculations, the imaginary time step needed to accurately approximate the many-body Green's function by the pair-product is $\tau = (2000 \text{ MeV})^{-1}$. For larger time steps, commutator terms in the Trotter breakup spoil the approximation. Since, in the pair product approximation, these commutators occur only when three nucleons are close together, this indicates that, three-body effects will also be important. That is, to be able to use the propagators in the limit where they become model independent, would likely require that three- and more-body terms in both the interaction and the propagators be included. This likely means that use of potentials like $V_{\text{low } k}$ for many-nucleon calculations will need to include many-body interactions.

IV. QUANTUM MONTE CARLO WITH NON-LOCAL POTENTIALS

We now turn to the central parts of the propagators for the non-local $N^3\text{LO}$ and $N^3\text{LO}(600)$ potentials we have been considering throughout. Since the central part of the propagator is sampled in a quantum Monte Carlo calculation it should be positive-definite to avoid sign problems.

Figures 10 and 11 plot the central part of the propagator in real space, where the coordinates x' and z' are such that the origin corresponds to the final separation equal to the initial separation. That is, the relative coordinates are equal: $r = r'$. The precise transformation between the original coordinates, r , r' , and θ' and the new coordinates, x' and z' is given by

$$r'^2 = x'^2 + (r + z')^2 \tag{19a}$$

$$\cos \theta' = \frac{r + z'}{\sqrt{x'^2 + (r + z')^2}}, \tag{19b}$$

and can be visualized in Fig. 12.

The structure we can see is a Gaussian-like peak about the initial separation as well as

an antisymmetric trough at the position that corresponds to the two nucleons undergoing a position interchange: $r' = -r$. The antisymmetric point is built in from tracing over the spins and isospins as in Eq. (12), and would be present even for Argonne v_{18} . This point gives no extra difficulty — since it comes from the fermion character of the nucleons, it will be dealt with in the same way that the fermion sign problem is dealt with in Green’s function or auxiliary field diffusion Monte Carlo. That is, a path constraint [25] is imposed that eliminates the fermion sign problem. The constraint can then be released and forward walking steps taken [25, 26] to improve the results and check the effect of the constraint.

However, if we zoom in on the shifted origin, as in Figs. 13, and 14, setting any positive parts of the propagator to zero, and make sure we are clear of the antisymmetric region, we find that the propagators appear to be “ringing”, much like Friedel oscillations. These negative parts may make it more difficult to perform quantum Monte Carlo calculations and keep the sign problem under control. However, these negative parts are quite small, of order 10^{-1} fm^{-3} , whereas the peak of the propagator is of order 10^2 fm^{-3} . In fact, a typical slice through the propagator in the x' direction looks like Figs. 15 and 16. In many cases, the negative parts are negligible.

A straightforward method to take the small negative regions into account, is to first set any negative part (not associated with the antisymmetry) to zero, run a quantum Monte Carlo calculation until it converges, and then add the negative parts back in, in a perturbative fashion, using forward walking exactly as for the fermion sign problem. The extra sign changes from the propagator are handled in the same way as sign changes from the fermion character.

We can estimate the fraction of walkers in the initial time step that may be given negative weights by comparing the integral of the absolute value of the propagators to the integral of the propagators. That is, we estimate the fraction of walkers with negative weights, f by

$$f = \frac{\int d^3r' \frac{1}{2} [|G(\mathbf{r}, \mathbf{r}'; \tau)| - G(\mathbf{r}, \mathbf{r}'; \tau)]}{\int d^3r' |G(\mathbf{r}, \mathbf{r}'; \tau)|}. \quad (20)$$

We calculate the integral over the upper half volume to exclude the interchange. For N³LO with an initial separation of 1.0 fm, we find $f \sim \mathcal{O}(10^{-2})$. If we now take the very conservative estimate for the alpha particle that all six pairs may be this close at one time and that the negative weights are acceptable so long as the fraction of walkers with negative weights is less than $1/e$, we find we can take approximately ten steps for N³LO [with time step

$(2000 \text{ MeV})^{-1}$]. Green’s function Monte Carlo typically uses forward walking of about 10 to 20 steps of $(2000 \text{ MeV})^{-1}$ [25, 26]. Therefore forward walking will allow us to remove any bias from the negative parts of the propagator. This can be compared to forward walking keeping the propagator constraint, but releasing the fermion constraint to separate the two effects.

In the above analysis, we have assumed that the imaginary time step used will be the same as that used in Green’s function Monte Carlo calculations with the Argonne family of potentials. Since the N³LO potentials are softer, the relevant commutators terms will be smaller, and longer time steps may be possible. For longer time steps there is much less ringing, and the calculations will be substantially easier.

V. CONCLUSIONS

We have shown how to calculate the imaginary time pair propagators needed for quantum Monte Carlo calculations of nuclei and nuclear matter using non-local potentials in momentum space. The method is general enough to handle any non-local potential in momentum or real space, but in this paper, we focus on those derived from effective field theory (N³LO).

We find that the propagators display a universal behavior at large imaginary times, consistent with our expectations from renormalization group methods and the fact that the potentials are phase-shift equivalent, meaning that they reproduce the scattering data at or below laboratory energies of 350 MeV.

The central propagators sampled during Monte Carlo simulations for local potentials are expected to be positive-definite. Without this property, sign problems can develop. We find that for N³LO with a 500 MeV or 600 MeV cutoff in momentum space, the central propagator is not positive definite. However, the negative parts consist of “rings” reminiscent of Friedel oscillations and their magnitude is quite small compared with the overall shape of the central propagator. Since these potentials were developed in momentum space, no attempt was made to influence their behavior in position space. It may be possible to modify the N³LO potentials in such a way that they continue to reproduce the Nijmegen data with a low χ^2 , are still relatively soft, but have reduced ringing behavior. A modification of the choice of the regulator function used in the calculation of the N³LO potentials: $V(k, k') \rightarrow V(k, k')e^{-(k/\Lambda)^{2\nu}}e^{-(k'/\Lambda)^{2\nu}}$, where Λ is the cutoff value, and ν is the order of the calculation,

($\nu = 4$ for N³LO) may help. In any case, quantum Monte Carlo calculations should still be possible by using a modified path constraint as described above, and we are implementing these calculations.

While we have concentrated on calculating the imaginary time pair propagators from phenomenological potentials, it is amusing to note that since the few-body imaginary time propagators are simply imaginary-time correlations of the appropriate nucleon operators, they might eventually be directly extracted from lattice QCD calculations.

ACKNOWLEDGMENTS

The authors would like to thank J. Carlson, R. J. Furnstahl, and S. Gandolfi for helpful conversations. This work was supported by the National Science Foundation under Grant No. PHY-1067777.

-
- [1] M. J. Savage, AIP Conf.Proc. **1343**, 30 (2011), arXiv:1012.0876 [nucl-th].
 - [2] S. R. Beane, W. Detmold, K. Orginos, and M. J. Savage, Progress in Particle and Nuclear Physics **66**, 1 (2011).
 - [3] D. Lee, in *Progress in Particle and Nuclear Physics, VOL 63, NO 1*, Progress in Particle and Nuclear Physics, Vol. 63, edited by Faessler, A (Elsevier Science BV, 2009) pp. 117–154.
 - [4] E. Epelbaum, H. Krebs, D. Lee, and U. G. Meissner, European Physical Journal A **45**, 335 (2010).
 - [5] E. Epelbaum, H. Krebs, D. Lee, and U.-G. Meißner, Phys. Rev. Lett. **106**, 192501 (2011).
 - [6] E. Epelbaum, Progress in Particle and Nuclear Physics **67**, 343 (2012).
 - [7] J. Carlson, Phys. Rev. C **36**, 2026 (1987).
 - [8] S. C. Pieper and R. B. Wiringa, Ann.Rev.Nucl.Part.Sci. **51**, 53 (2001), arXiv:nucl-th/0103005 [nucl-th].
 - [9] K. E. Schmidt and S. Fantoni, Phys. Lett. B **446**, 99 (1999).
 - [10] S. Gandolfi, F. Pederiva, S. Fantoni, and K. E. Schmidt, Phys. Rev. Lett. **98**, 102503 (2007).
 - [11] S. Gandolfi, F. Pederiva, S. Fantoni, and K. E. Schmidt, Phys. Rev. Lett. **99**, 022507 (2007).
 - [12] R. B. Wiringa, V. Stoks, and R. Schiavilla, Phys.Rev. **C51**, 38 (1995),

- arXiv:nucl-th/9408016 [nucl-th].
- [13] J. Carlson, V. Pandharipande, and R. B. Wiringa, Nucl.Phys. **A401**, 59 (1983).
 - [14] S. C. Pieper, V. Pandharipande, R. B. Wiringa, and J. Carlson, Phys.Rev. **C64**, 014001 (2001), arXiv:nucl-th/0102004 [nucl-th].
 - [15] P. Navratil, J. P. Vary, and B. R. Barrett, Phys.Rev. **C62**, 054311 (2000).
 - [16] P. Navratil, S. Quaglioni, I. Stetcu, and B. R. Barrett, Journal of Physics G: Nuclear and Particle Physics **36**, 083101 (2009).
 - [17] G. Hagen, T. Papenbrock, D. J. Dean, and M. Hjorth-Jensen, Phys. Rev. C **82**, 034330 (2010).
 - [18] G. R. Jansen, M. Hjorth-Jensen, G. Hagen, and T. Papenbrock, Phys. Rev. C **83**, 054306 (2011).
 - [19] G. Hagen, T. Papenbrock, D. Dean, and M. Hjorth-Jensen, Phys.Rev.Lett. **101**, 092502 (2008), arXiv:0806.3478 [nucl-th].
 - [20] D. Entem and R. Machleidt, Phys.Rev. **C68**, 041001 (2003), arXiv:nucl-th/0304018 [nucl-th].
 - [21] D. Ceperley, Rev. Mod. Phys. **67**, 279 (1995).
 - [22] B. S. Pudliner, V. R. Pandharipande, J. Carlson, S. C. Pieper, and R. B. Wiringa, Phys. Rev. C **56**, 1720 (1997).
 - [23] S. Bogner, T. Kuo, A. Schwenk, D. Entem, and R. Machleidt, Phys.Lett. **B576**, 265 (2003), arXiv:nucl-th/0108041 [nucl-th].
 - [24] S. Bogner, R. Furnstahl, and R. Perry, Phys.Rev. **C75**, 061001 (2007), arXiv:nucl-th/0611045 [nucl-th].
 - [25] R. B. Wiringa, S. C. Pieper, J. Carlson, and V. R. Pandharipande, Phys. Rev. C **62**, 014001 (2000).
 - [26] S. C. Pieper, K. Varga, and R. B. Wiringa, Phys. Rev. C **66**, 044310 (2002).

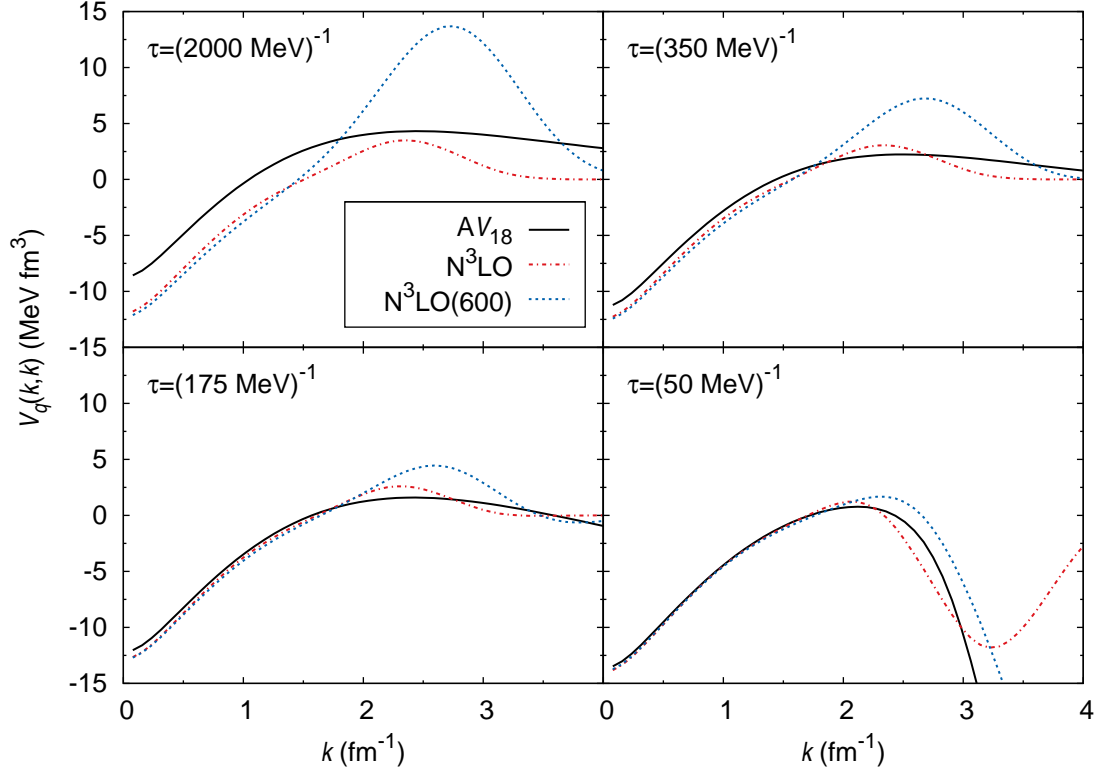


FIG. 1. (color online) The quantum potential in the 1S_0 partial wave in momentum space as the propagator is calculated for successively longer imaginary times.

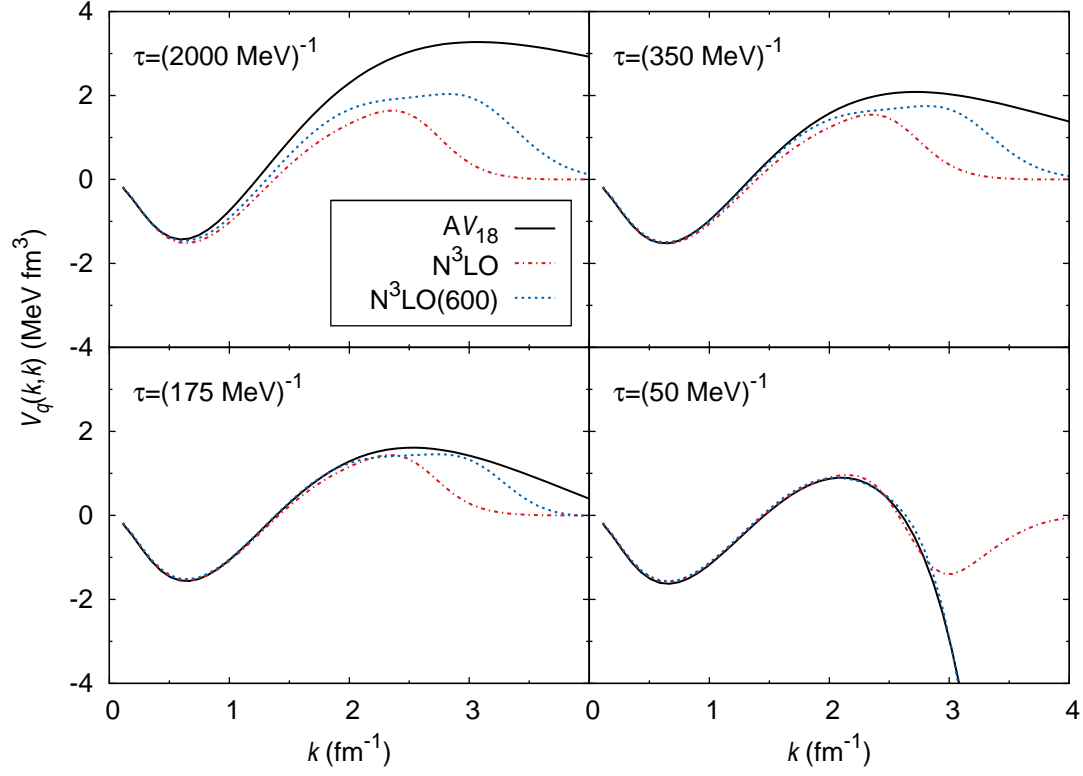


FIG. 2. (color online) The quantum potential in the 3P_0 partial wave in momentum space as the propagator is calculated for successively longer imaginary times.

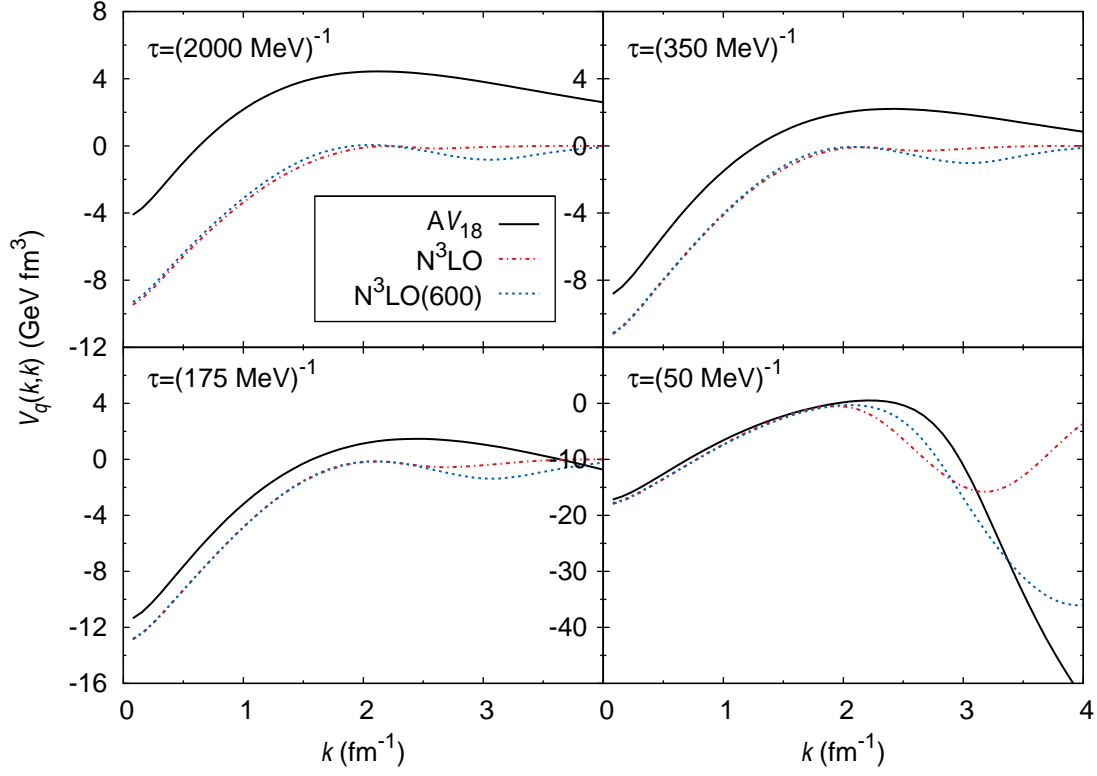


FIG. 3. (color online) The quantum potential in the 3S_1 partial wave as the propagator is calculated for successively longer imaginary times.

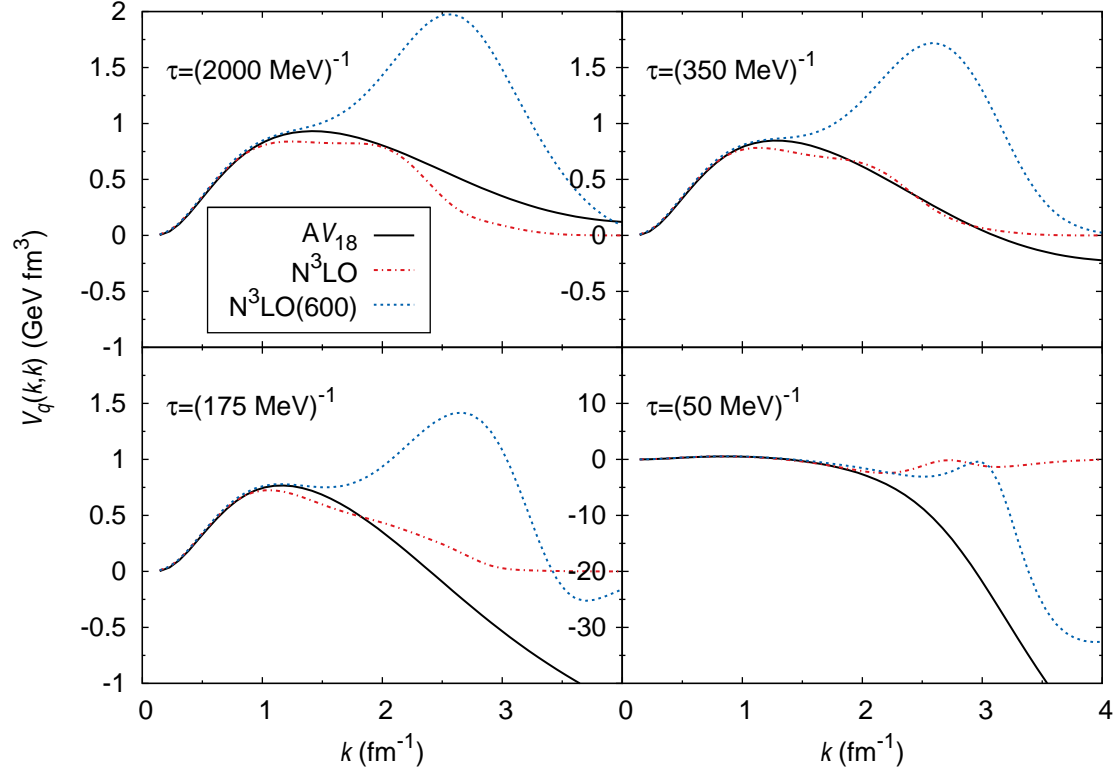


FIG. 4. (color online) The quantum potential in the 3D_1 partial wave as the propagator is calculated for successively longer imaginary times.

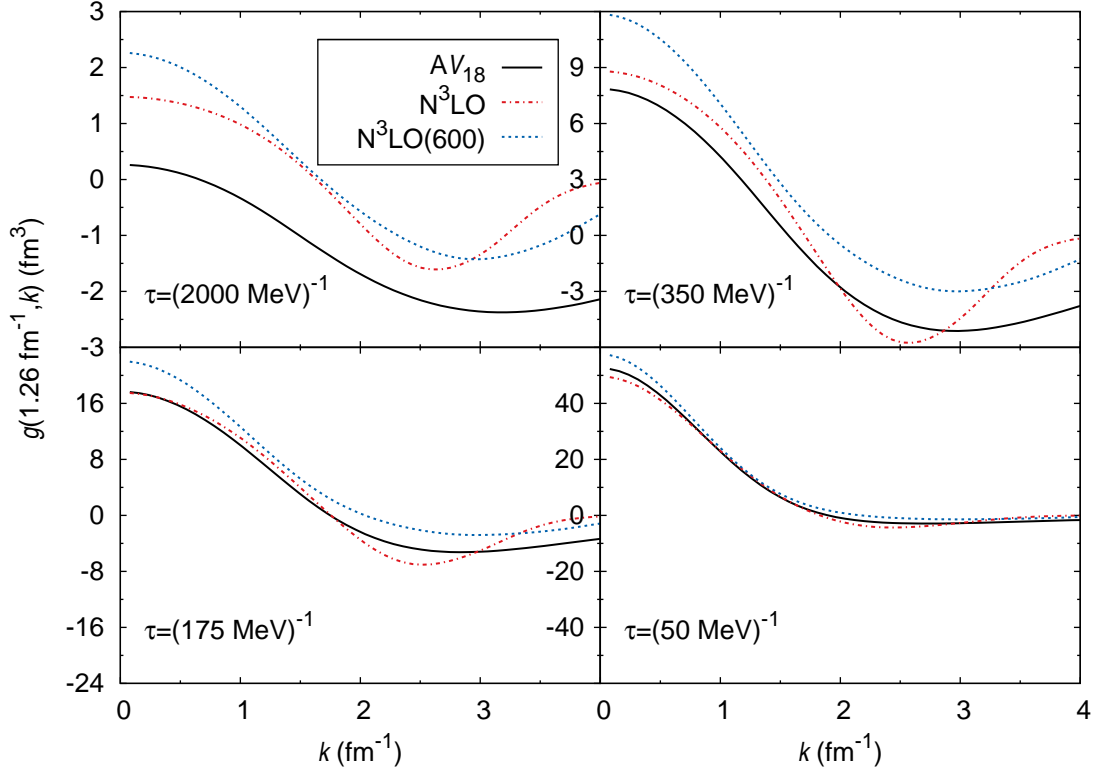


FIG. 5. (color online) The off-diagonal momentum-space propagator (minus the free-particle propagator) in the 1S_0 partial wave as the propagator is calculated for successively longer imaginary times.

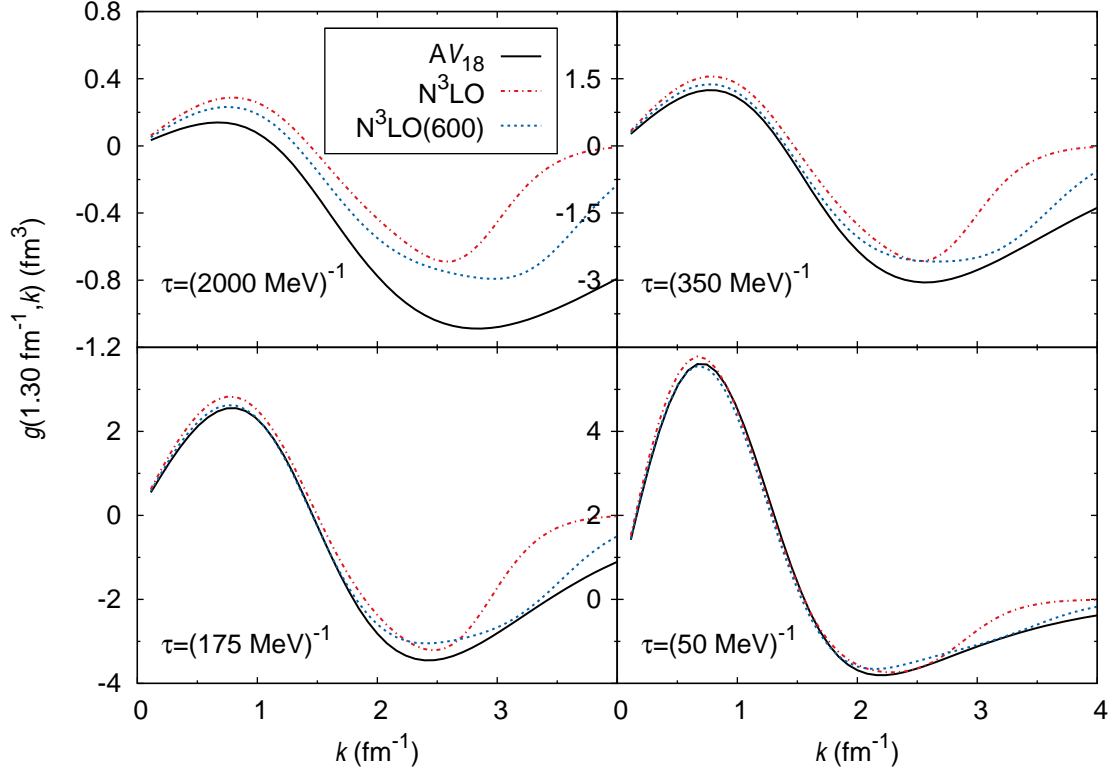


FIG. 6. (color online) The off-diagonal momentum-space propagator (minus the free-particle propagator) in the 3P_0 partial wave as the propagator is calculated for successively longer imaginary times.

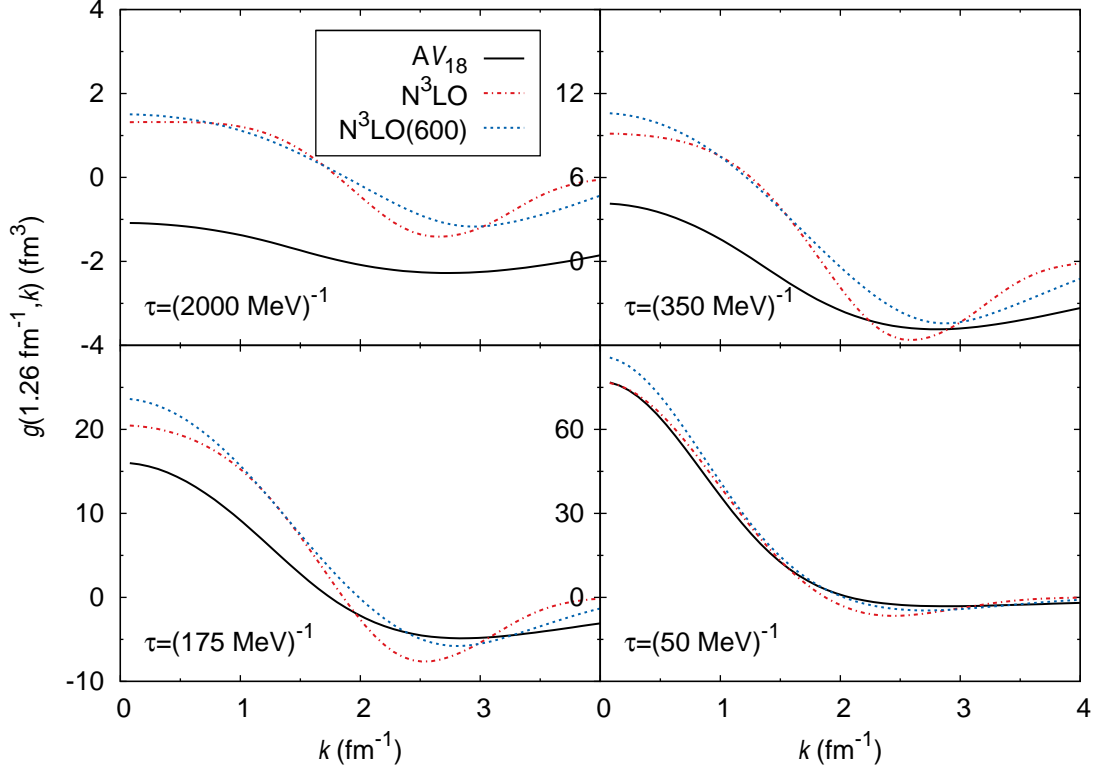


FIG. 7. (color online) The off-diagonal momentum-space propagator (minus the free-particle propagator) in the 3S_1 partial wave as the propagator is calculated for successively longer imaginary times.

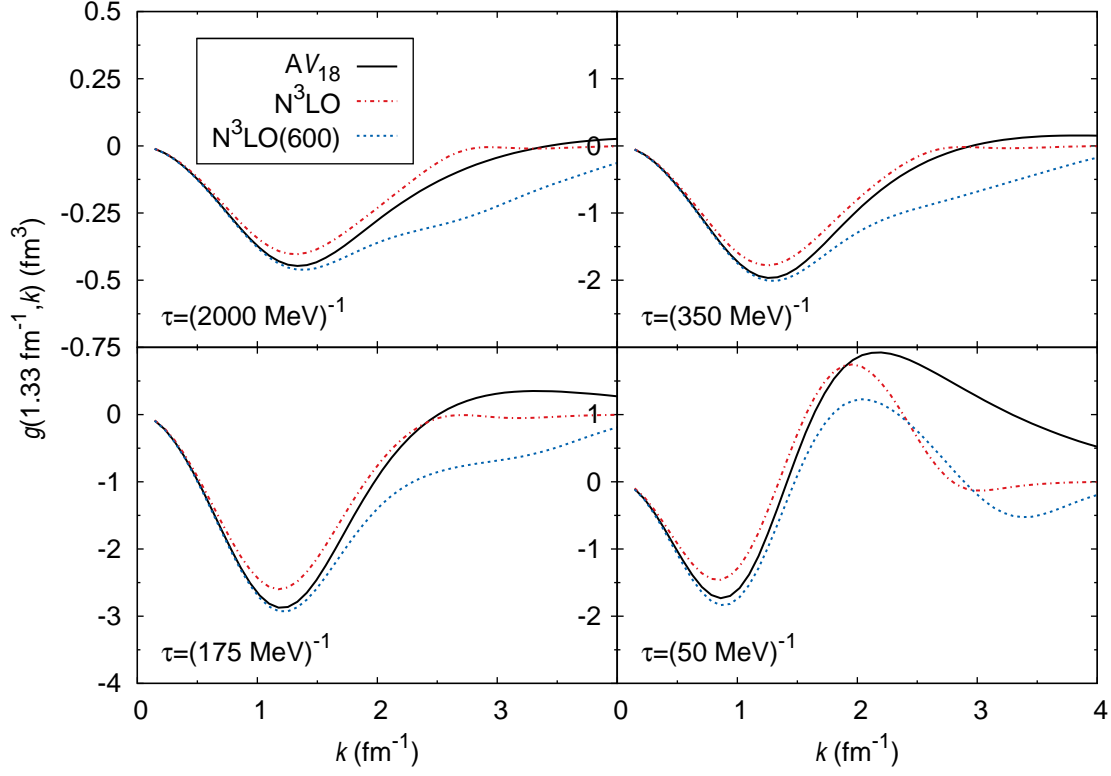


FIG. 8. (color online) The off-diagonal momentum-space propagator (minus the free-particle propagator) in the 3D_1 partial wave as the propagator is calculated for successively longer imaginary times.

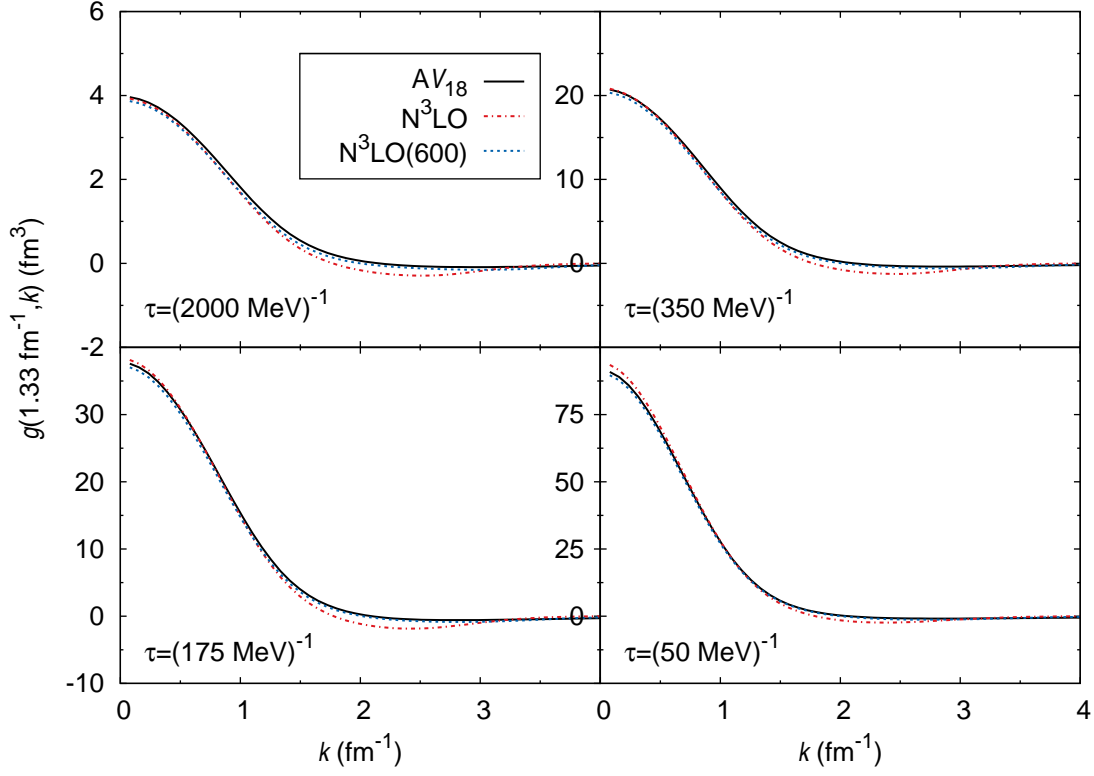


FIG. 9. (color online) The off-diagonal momentum-space propagator (minus the free-particle propagator) in the 3S_1 - 3D_1 partial wave as the propagator is calculated for successively longer imaginary times.

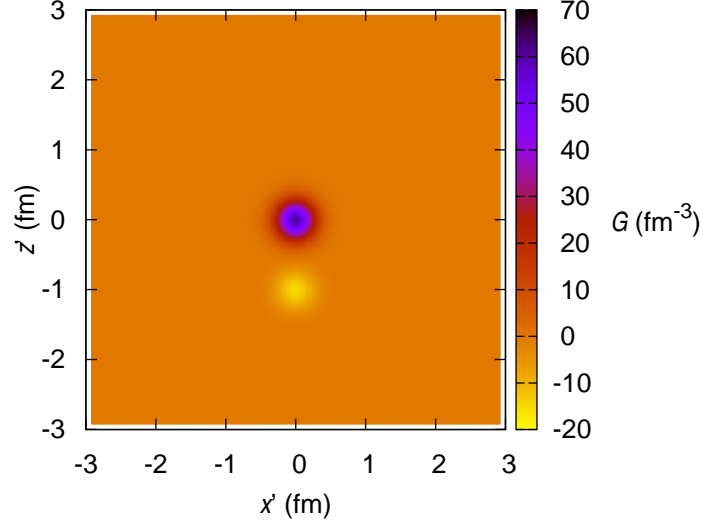


FIG. 10. (color online) The N^3LO central propagator for initial separation, $r = 0.5$ fm, and imaginary time, $\tau = (2000 \text{ MeV})^{-1}$.

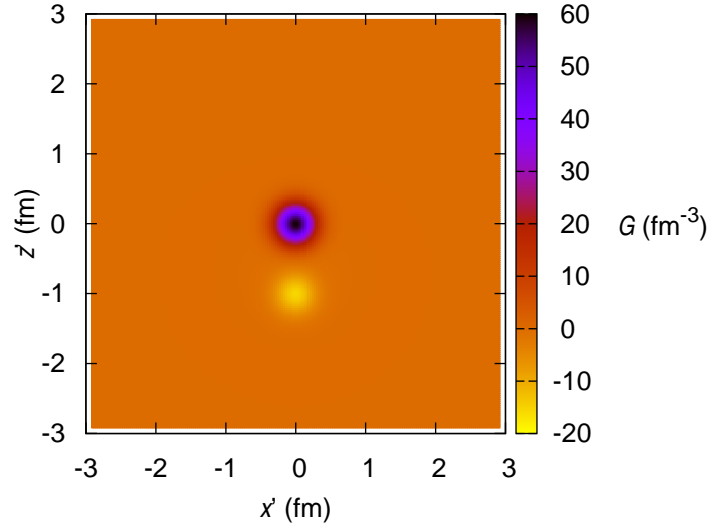


FIG. 11. (color online) The $\text{N}^3\text{LO}(600)$ central propagator for initial separation, $r = 0.5$ fm, and imaginary time, $\tau = (2000 \text{ MeV})^{-1}$.

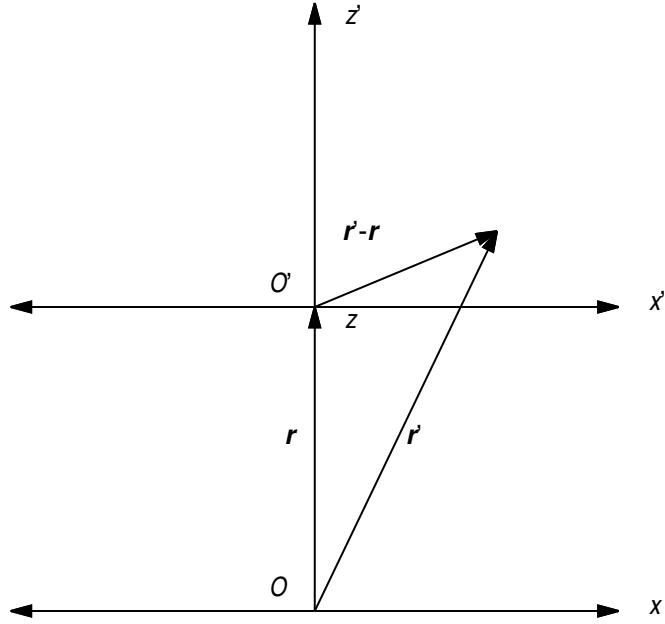


FIG. 12. The coordinate system used to visualize the central propagators. O is the original origin, and O' the shifted origin such that $r = r'$ corresponds to the shifted origin.

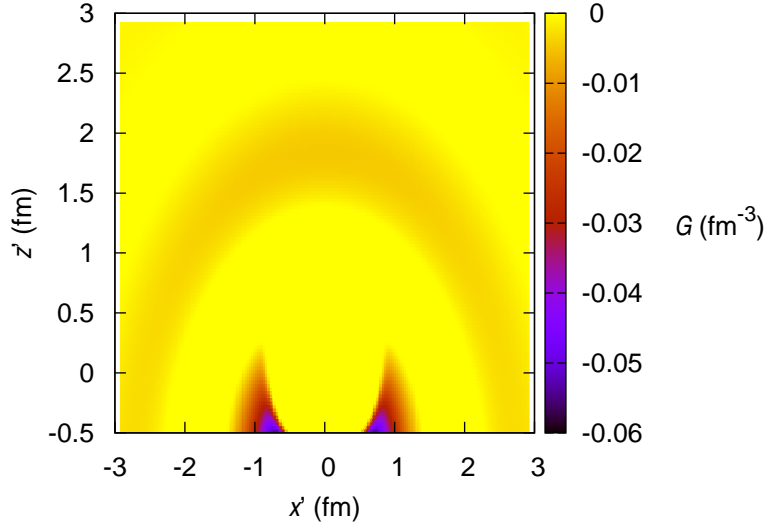


FIG. 13. (color online) The negative parts of the $N^3\text{LO}$ central propagator for initial separation, $r = 0.5$ fm, and imaginary time, $\tau = (2000 \text{ MeV})^{-1}$.

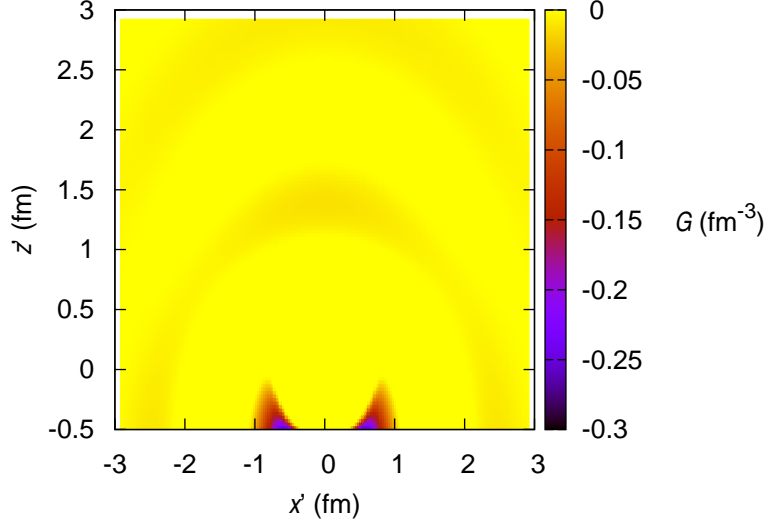


FIG. 14. (color online) The negative parts of the $N^3\text{LO}(600)$ central propagator for initial separation, $r = 0.5$ fm, and imaginary time, $\tau = (2000 \text{ MeV})^{-1}$.

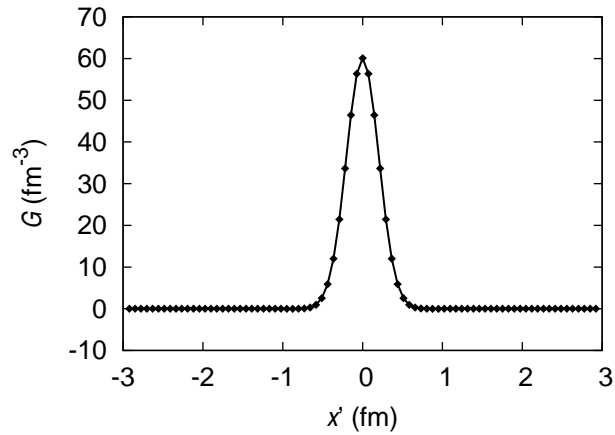


FIG. 15. A typical slice through the $N^3\text{LO}$ central propagator for initial separation, $r = 0.5$ fm, and imaginary time, $\tau = (2000 \text{ MeV})^{-1}$.

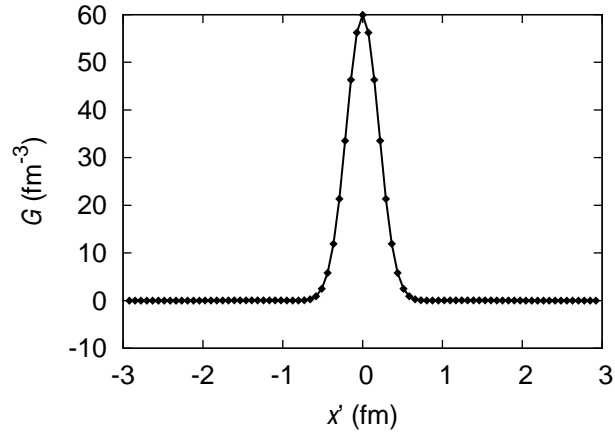


FIG. 16. A typical slice through the $N^3\text{LO}(600)$ central propagator for initial separation, $r = 0.5$ fm, and imaginary time, $\tau = (2000 \text{ MeV})^{-1}$.